Article:
Wirths, S, Geiger, R, von den Driesch, N et al. (2015) Lasing in direct-bandgap GeSn alloy grown on Si. Nature Photonics, 9 (2). 88 - 92. ISSN: 1749-4885

https://doi.org/10.1038/nphoton.2014.321

Lasing in direct bandgap GeSn alloy grown on Si (001)

S. Wirths[1*†], R. Geiger[2,3†], N. von den Driesch[1], G. Mussler[1], T. Stoica[1], S. Mantl[1], Z. Ikonic[4], M. Luysberg[5], S. Chiussi[6], J.M. Hartmann[7], H. Sigg[2], J.Faist[3], D. Buca[1] and D. Grützmacher[1]

[1]Peter Grünberg Institute 9 (PGI 9) and JARA-Fundamentals of Future Information Technologies, Forschungszentrum Juelich, 52425 Juelich, Germany

[2]Laboratory for Micro- and Nanotechnology (LMN), Paul Scherrer Institut, CH-5232 Villigen, Switzerland

[3]Institute for Quantum Electronics, ETH Zürich, CH-8093 Zürich, Switzerland

[4]Institute of Microwaves and Photonics, School of Electronic and Electrical Engineering, University of Leeds, Leeds LS2 9JT, United Kingdom

[5]Peter Grünberg Institute 5 (PGI 5) and Ernst Ruska-Centrum, Forschungszentrum Juelich, 52425 Juelich, Germany

[6]Dpto. Física Aplicada, E.E.Industrial, Univ. de Vigo, Campus Universitario, 36310 Vigo, Spain

[7]Univ. Grenoble Alpes, F-38000 Grenoble, France

CEA, LETI, MINATEC Campus, F-38054 Grenoble, France

[*]e-mails: s.wirths@fz-juelich.de; d.m.buca@fz-juelich.de

[†]These authors contributed equally to this work.

Large-scale optoelectronics integration is limited by silicon's inability to emit light efficiently[1], since Si and the chemically well-matched Ge are indirect bandgap semiconductors. In order to overcome this drawback, several routes have been followed, such as the all-optical Si Raman laser[2] or the heterogeneous integration of direct bandgap III-V lasers on Si[3-7]. Here, we report on lasing in a direct bandgap group IV system created by alloying Ge with Sn[8] without mechanically introducing strain[9,10]. Strong enhancement of photoluminescence emerging from the direct transition with decreasing temperature is the signature of a fundamental direct bandgap semiconductor. For T ≤ 90 K, the observation of a threshold in emitted intensity with increasing incident optical power, together with a strong linewidth narrowing and a consistent longitudinal cavity mode pattern highlights unambiguous laser action[11]. Direct bandgap group IV materials may thus represent a pathway towards the monolithic integration of Si-photonic circuitry and CMOS technology.

Although a group IV direct bandgap material has not been demonstrated yet, silicon photonics using CMOS-compatible processes has made great progress through the development of Si-based waveguides[12], photodetectors[13] and modulators[14]. The thus emerging technology is rapidly expanding the landscape of photonics applications towards tele- and data communication as well as sensing from the infrared to the mid infrared wavelength range[15-17]. Today's light sources of such systems are lasers made from direct bandgap group III-V materials operated off- or on-chip which requires fibre coupling or heterogeneous integration, for example by wafer bonding[3], contact printing[4,5] or direct growth[6,7], respectively. Hence, a laser source made of a direct bandgap group IV material would further boost lab-on-a-chip and trace gas sensing[15] as well as optical interconnects[18] by enabling monolithic integration. In this context, Ge plays a prominent role since the conduction band minimum at the Γ-point of the Brillouin-zone (referred to as Γ-valley) is located only approx. 140 meV above the fourfold degenerate indirect L-valley. To compensate for this energy difference and thus form a laser gain medium, heavy n-type doping of slightly tensile strained Ge has been proposed[19]. Later, laser action has been reported for optically[20] and electrically pumped Ge[21] doped to approx. 1 and 4×10^{19} cm^{-3}, respectively. However, pump-probe measurements of similarly doped and strained material did not show evidence for net gain[22], and in spite of numerous attempts, researchers failed to substantiate above results up to today. Other investigated concepts concern the engineering of the Ge band structure towards a direct bandgap semiconductor using micromechanically-stressed Ge nanomembranes[9] or silicon nitride (Si_3N_4) stressor layers[23]. Very recently, Süess *et al.*[10] presented a stressor-free technique which enables the introduction of more than 5.7 %[24] uniaxial tensile strain in Ge μ-bridges via selective wet under-etching of a pre-stressed layer. An alternative technique in order to achieve direct bandgap material is to incorporate Sn atoms into a Ge lattice, which primarily reduces the gap at the Γ-point. At a sufficiently high fraction of Sn, the energy of the Γ-valley decreases below that of the L-valley. This indirect-to-direct transition for relaxed GeSn binaries has been predicted to occur at about 20 % Sn by Jenkins *et al.*[25], but more recent calculations indicate much lower required Sn concentrations in the range of 6.5-11.0 %[26,27]. A major challenge for the realization of such GeSn alloys is the low (< 1 %) equilibrium solubility of Sn in Ge[28] and the large lattice mismatch of about 15 % between Ge and α-Sn. For GeSn grown on Ge substrates, this mismatch induces biaxial compressive strain causing a shift of the Γ− and L-valley crossover towards higher Sn concentrations[27]. Hence, strategies were adopted to obtain partially and also fully relaxed GeSn layers on Si[29] and on lattice matched InGaAs ternary alloy[30], respectively. Here we adopt the partial relaxation of up to 560 nm thick layers of GeSn on Ge/Si(001)-virtual substrates (Ge-VS).

For this study, we have investigated five samples (A to E) that have been grown using an industry-compatible 200 mm wafer reduced pressure CVD AIXTRON TRICENT® reactor and Ge_2H_6 and $SnCl_4$ precursors[31,32]. The GeSn layer thickness is 200-300 nm for samples A to D and 560 nm for sample E. The Sn concentrations (c.f. Table I) were determined by Rutherford backscattering spectrometry (RBS, see Fig. S1, SI) and X-ray diffraction reciprocal space mapping (XRD-RSM) (details in SI). The Ge buffer layers grown at 400/750°C contain a weak biaxial tensile strain of 0.16 % at room temperature (RT) due to the different thermal expansion coefficients of Si and Ge. The strain levels as well as Sn concentrations in the partially relaxed GeSn layers are summarized in Table I. The latter have been determined from a modified version of Vegard's law[33]. The experimentally determined Sn concentration and the strain have been used to calculate the electronic bandgaps at RT (c.f. Fig. S2, SI). Sample A containing approx. 8 % Sn is expected to be an indirect bandgap semiconductor since the L-valley is well below the Γ-valley in energy. For samples B and C, the difference between Γ- and L-valley (c.f. Table I) is smaller than k_BT at room temperature. According to the calculation, the -0.71 % strained sample D exhibits a fundamental direct bandgap with the Γ-valley being 28 meV below the indirect L-valley. Sample E is a replica of sample D apart from the epilayer thickness that has been increased to improve the overlap between the optical mode and the gain material.

Cross sectional transmission electron microscopy (XTEM) micrographs (Fig. 1a, b) of sample D (12.6 % Sn) show high crystalline quality of the GeSn layer and reveal a high density of misfit dislocations at the interface (orange arrows). Part of the plastic relaxation occurred through creation of dislocation half-loops (blue arrows) extending into the Ge buffer layer. High-resolution imaging (see Fig. 1c) shows that most of the misfit dislocations at an average spacing of 12.5 nm are pure edge dislocations with a Burgers vector a/2 [110]. These so-called Lomer dislocations are the most efficient type of dislocation to induce strain relaxation[34]. The fact that no threading dislocation reached the sample surface in any of the examined TEM samples allows an estimate of the upper limit of the threading dislocation density (TDD) of 5×10^{6} cm^{-2}.

In order to prove whether the bandgap is fundamental direct or indirect, temperature-dependent photoluminescence (PL) measurements (c.f. Methods) were performed. In Figure 2a, PL spectra in the range from 20 to 300 K are shown for four different GeSn alloys (samples A-D). Note that the ordinate is fixed in order to facilitate the comparison of peak intensities. Going from sample A at room temperature to sample D at 20 K, the peak intensity increases approximately 350 times. This enormous gain in intensity is a combined consequence of sample cooling and inversion of the band offset between Γ– and L-valleys. The weak, broad luminescence observed around 0.4 eV at lower temperatures might stem from misfit dislocations formed at the GeSn/Ge interface discussed above. The PL intensity of the main peak is linearly related to the excitation power which is characteristic for a dominant band-to-band recombination (see Fig. S3, SI). Figure 2b presents the integrated PL intensity as a function of temperature. The curves are normalized to unity at 300 K. For 8 % Sn (sample A), the Γ-valley-emission intensity strongly decreases with decreasing temperature which is typical for Ge[35] and low Sn content GeSn alloys[36]. The Γ-valley luminescence of sample D is steadily increasing by about two orders of magnitude with decreasing temperature from 300 K to 20 K. This change in behaviour is consistent with the fundamental bandgap being direct. The temperature dependence of the integrated PL intensities of samples B and C are more complex. For temperatures ≥ 150 K, the intensities remain nearly constant, whereas they slightly increase for T ≤ 150 K. The explanation involves the application of a joint density of states (JDOS) model (for details see SI) including calculated effective masses and valence band parameters (Table S1 and S2 in SI). The energy difference ΔE between the Γ- and L-valley is used as a fitting parameter together with the optically injected carrier density, $n_C(T) = \frac{n_0}{\tau_0} \cdot \tau(T)$, where n_0 represents the density of carriers at room temperature, $\tau(T)$ the temperature-dependent recombination time and $\tau_0 = \tau(300\ K)$. For the fit we assume $\tau(T)$ (i) to be identical for all samples, and (ii) to resemble that of the Shockley-Read-Hall (SRH) recombination process (see SI). An excellent fit of the T-dependence of the PL intensity is displayed in Fig. 2b. We also find that $n_0 = 4\times10^{17}$ cm^{-3} which agrees with the excitation density (c.f. Methods) and a τ_0 of 0.35 ns corresponding to a surface recombination velocity of 570 m/s. Similar relaxation times have been measured for elemental Ge[37] supporting the high crystalline quality of our GeSn layers. In the fit of sample D the Γ-valley lies 25 meV below the L-valley, in excellent agreement with the prediction of a fundamental direct bandgap. For sample A, the experiments reveal a clear indirect bandgap with an -80 meV offset compared to the prediction of ΔE = - 50 meV. In order to extract the dependence of the conduction band offset on the Sn concentration, x_{Sn}, the measured values were extrapolated to a strain of 0 % using ΔE = 7.7 eV per unit strain following the model calculations. The direct bandgap as revealed by experiment is, therefore, reached for fully relaxed samples for Sn concentrations exceeding about 9%, which is in fair agreement with the theoretical prediction shown by the green line in Fig. 2c.

As we will show in the remaining part of this letter, sample E (which is the thicker pendant of layer D, c.f. Figure S5 in SI) provides sufficient optical gain to enable lasing. For the gain measurement, the luminescence is collected from the edge of a several mm long and 5 µm wide waveguide (WG) structure that is excited over the variable length *L* by a 5 ns long laser pulse at 1064 nm wavelength.

In Fig. 3a, PL spectra at 20 K and an optical excitation of 595 kW/cm^2 for different stripe lengths are shown, revealing a more than linear increase of the intensity and a substantial decrease in linewidth for increasing stripe lengths *L,* plotted in Fig. 3b. As expected, the PL emission energy of sample E (approx. 0.55 eV, which corresponds to a wavenumber and wavelength of 4435 cm^{-1} and 2.25 μm, respectively) closely matches the one observed for sample D. The emission shifts to the blue with increasing excitation power, c.f. Fig. 3b. The inset of Fig. 3a indicates an overlap of the fundamental mode with the GeSn layer of almost 60 % (c.f. Table S3 in SI). The modal gain g, which includes waveguide losses is determined for four different excitations from[38] $I_{ASE} = I_{O.}+I_{SP.}/g\cdot[\exp(g\cdot L)-1]$, as displayed in the lower part of Fig. 3b where I_{ASE} and $I_{SP.}$ refer to the amplified- and unamplified spontaneous emission, respectively. $I_{O.}$ contains contributions from the excited (but not amplified) higher order modes as well as light collected from the sidewalls. We limited the gain analysis to excitations < 600 kW/cm^2 and lengths ≤ 550 μm to avoid the stimulated feedback of backwards-reflected light from the WG sidewalls. The obtained modal gain as a function of pump energy is plotted in Fig. 3c; a differential gain of (0.40 ± 0.04) cm/kW is obtained from the slope. By extrapolation to the gain onset, we obtain a threshold excitation density of approximately 325 kW/cm^2.

By exciting over the full length of a 1 mm long WG and, hence, employing the multiple reflections feedback from the WG facets forming a Fabry-Perot cavity (c.f. inset of Fig. 4c), an unambiguous proof of lasing can be seen in Figure 4a as a distinct threshold in output intensity. Once this threshold is exceeded, the FWHM decreases and the emission intensity increases dramatically, as displayed in Figure 4b. The laser intensity increase flattens at approx. 650 kW/cm^2, which we attribute to sample heating. Shot-to-shot fluctuations of the excitation power are the reason that the lasing onset lies slightly below the gain onset as found from the variable stripe length measurement. Likewise, the modal gain as estimated from the reflection losses using $\alpha = 1/L \cdot \ln(1/R)$ with the reflectivity R appears at lower average excitation values according to Figure 3c. At 1000 kW/cm^2 peak excitation, lasing was observed up to 90 K (inset of Figure 4a). This temperature coincides with the activation temperature for the SRH recombination (see SI Figure S4). Hence, we tentatively ascribe the threshold degradation as well as the still low external differential quantum efficiency of an estimated 1.5 % (see Fig. S6, SI) to a reduced carrier lifetime due to as yet unidentified extrinsic recombination centres along with the small energy separation between Γ- and L-valleys and valence interband absorption[22]. The operating temperature and lasing efficiency can be improved by introducing heterostructure layers comprising GeSnSi/GeSn[31] for carrier confinement, and by n-doping[19].

In Figure 4c, we present a final piece of evidence for lasing[11] by showing the Fabry-Perot oscillations observed in a 250 and 500 μm long WG structure, respectively. From the oscillation period, a group mode refractive index of 4.5 is deduced which reflects the dispersion of the refractive index in the pumped GeSn as well as in the Ge substrate[37].

In summary, we present detailed PL studies performed on high quality, partially strain-relaxed GeSn layers with Sn concentrations of up to 12.6 % grown on Ge buffered Si(001) substrates. Structural investigations exhibit a low density of threading dislocations, homogenously distributed Sn atoms and mild compressive strain levels facilitated by a particularly favourable relaxation mechanism. The existence of a direct bandgap group IV semiconductor is shown that exhibits modal gain. Fabry-Perot resonators are fabricated, permitting the demonstration of lasing under optical pumping. Owing to the striking relation between the SRH recombinations and laser quenching at ~ 90 K, surface passivation and design optimization regarding doping, optical mode confinement and carrier injection will help to increase the operation temperature as well as decrease the threshold excitation density. In a forthcoming development, electrical injection in therefor optimized SiGeSn/GeSn/SiGeSn double heterostructures[15,31] will be fabricated. In conclusion, although lasing is achieved at low temperatures and relatively high optical pumping, this demonstration of a direct bandgap group IV laser on Si(001) represents a promising proof-ofprinciple for a CMOS compatible gain material platform for cost-effective integration of electronic and photonic circuits.

Methods

GeSn layers were grown on thick Ge/Si virtual substrates employing an AIXTRON Tricent® reduced pressure CVD. Growth temperatures were chosen between 350 and 390°C, at rates between 17 and 49 nm/min.

The band structure around the Γ point was calculated by the 8 band k.p method including strain effects. Indirect conduction band valleys split with the applied strain, as described via appropriate deformation potentials. The parameters used are given in S.I. in Table S1.

For PL spectroscopy, a continuous-wave solid-state laser emitting at a wavelength of 532 nm with a power of 2 mW was focused to a spot size of ≈ 5 µm using a 15× Schwarzschild objective (*NA* = 0.4). The emitted luminescence was collected by the same objective, spectrally analysed using a Fourier transform infrared spectrometer and detected using a liquid nitrogen-cooled InSb detector with cut-off at 0.27 eV. The samples were mounted in a helium cold-finger cryostat. Steep, 900 nm deep sidewalls and facets of the WG were fabricated using an SF_6/C_4F_8-based reactive ion etching (RIE) process. The gain measurements and lasing demonstration were obtained using a pulsed laser (5 ns) emitting at 1064 nm wavelength and focused via a cylindrical lens onto a variable slit imaged 1:1 onto the sample by a biconvex lens.

Cross sectional TEM specimen have been prepared by means of a dual-beam focused ion beam FIB (FEI Helios Nanolab 400S) operated at 30 and 5 kV. A 3 µm thick Pt/C protective layer was deposited on the surface of the sample prior to FIB milling. Surface damage created by Ga ions were reduced by low-energy (<1 kV) Ar ion milling using the Fischione Instruments Model 1040 Nanomill system. Conventional and high-resolution images have been recorded using an aberration-corrected (fourth order) FEI Titan 80-300 transmission electron microscope operated at 300 kV.

References

1. Iyer, S. S. & Xie, Y. H. Light emission from silicon. *Science* **260,** 40–6 (1993).

2. Rong, H. *et al.* An all-silicon Raman laser. *Nature* **433,** 292–4 (2005).

3. Fang, A. W. *et al.* Electrically pumped hybrid AlGaInAs-silicon evanescent laser. *Opt. Express* **14,** 9203–10 (2006).

4. Justice, J. *et al.* Wafer-scale integration of group III–V lasers on silicon using transfer printing of epitaxial layers. *Nat. Photonics* **6**, 612–616 (2012).

5. Yang, H. *et al.* Transfer-printed stacked nanomembrane lasers on silicon. *Nat. Photonics* **6**, 617–622 (2012).

6. Liu, H. *et al.* Long-wavelength InAs/GaAs quantum-dot laser diode monolithically grown on Ge substrate. *Nat. Photonics* **5,** 416–419 (2011).

7. Chen, R. *et al.* Nanolasers grown on silicon. *Nat. Photonics* **5**, 170–175 (2011).

8. Chen, R. *et al.* Demonstration of a Ge/GeSn/Ge quantum-well microdisk resonator on silicon: enabling high-quality Ge(Sn) materials for micro- and nanophotonics. *Nano Lett.* **14,** 37–43 (2014).

9. Sánchez-Pérez, J. R. *et al.* Direct-bandgap light-emitting germanium in tensilely strained nanomembranes. *Proc. Natl. Acad. Sci. U. S. A.* **108,** 18893–8 (2011).

10. Süess, M. J. *et al.* Analysis of enhanced light emission from highly strained germanium microbridges. *Nat. Photonics* **7,** 466–472 (2013).

11. Samuel, I. D. W., Namdas, E. B. & Turnbull, G. A. How to recognize lasing. *Nat. Photonics* **3,** 546–549 (2009).

12. Xia, F., Sekaric, L. & Vlasov, Y. Ultracompact optical buffers on a silicon chip. *Nat. Photonics* **1,** 65–71 (2007).

13. Assefa, S., Xia, F. & Vlasov, Y. A. Reinventing germanium avalanche photodetector for nanophotonic on-chip optical interconnects. *Nature* **464,** 80–4 (2010).

14. Xu, Q., Schmidt, B., Pradhan, S. & Lipson, M. Micrometre-scale silicon electro-optic modulator. *Nature* **435,** 325–7 (2005).

15. Soref, R. Mid-infrared photonics in silicon and germanium. *Nat. Photonics* **4,** 495–497 (2010).

16. Roelkens, G. *et al.* Silicon-Based Photonic Integration Beyond the Telecommunication Wavelength Range. *IEEE J. Sel. Top. Quantum Electron.* **20,** 394–404 (2014).

17. Duan, G.-H. *et al.* Hybrid III-V on Silicon Lasers for Photonic Integrated Circuits on Silicon. *IEEE J. Sel. Top. Quantum Electron.* **20,** 158–170 (2014).

18. Heck, M. J. R. & Bowers, J. E. Energy Efficient and Energy Proportional Optical Interconnects for Multi-Core Processors: Driving the Need for On-Chip Sources. *IEEE J. Sel. Top. Quantum Electron.* **20,** 1–12 (2014).

19. Liu, J. *et al.* Tensile-strained, n-type Ge as a gain medium for monolithic laser integration on Si. *Opt. Express* **15,** 11272–7 (2007).

20. Liu, J., Sun, X., Camacho-Aguilera, R., Kimerling, L. C. & Michel, J. Ge-on-Si laser operating at room temperature. *Opt. Lett.* **35,** 679–81 (2010).

21. Camacho-Aguilera, R. E. *et al.* An electrically pumped germanium laser. *Opt. Express* **20,** 11316–20 (2012).

22. Carroll, L. *et al.* Direct-Gap Gain and Optical Absorption in Germanium Correlated to the Density of Photoexcited Carriers, Doping, and Strain. *Phys. Rev. Lett.* **109,** 057402 (2012).

23. De Kersauson, M. *et al.* Optical gain in single tensile-strained germanium photonic wire. *Opt. Express* **19,** 17925–34 (2011).

24. Sukhdeo, D. S., Nam, D., Kang, J.-H., Brongersma, M. L. & Saraswat, K. C. Direct bandgap germanium-on-silicon inferred from 5.7% <100> uniaxial tensile strain. *Photonics Res.* **2,** A8 (2014).

25. Jenkins, D. & Dow, J. Electronic properties of metastable Ge_xSn_{1-x} alloys. *Phys. Rev. B* **36,** 7994–8000 (1987).

26. Lu Low, K., Yang, Y., Han, G., Fan, W. & Yeo, Y. Electronic band structure and effective mass parameters of $Ge_{1-x}Sn_x$ alloys. *J. Appl. Phys.* **112,** 103715 (2012).

27. Gupta, S., Magyari-Köpe, B., Nishi, Y. & Saraswat, K. C. Achieving direct band gap in germanium through integration of Sn alloying and external strain. *J. Appl. Phys.* **113,** 073707 (2013).

28. He, G. & Atwater, H. A. Interband Transitions in Sn_xGe_{1-x} Alloys. *Phys. Rev. Lett.* **79,** 1937–1940 (1997).

29. Grzybowski, G. *et al.* Next generation of $Ge_{1-y}Sn_y$ (y = 0.01-0.09) alloys grown on Si(100) via Ge_3H_8 and SnD_4: Reaction kinetics and tunable emission. *Appl. Phys. Lett.* **101,** 072105 (2012).

30. Chen, R. *et al.* Increased photoluminescence of strain-reduced, high-Sn composition $Ge_{1-x}Sn_x$ alloys grown by molecular beam epitaxy. *Appl. Phys. Lett.* **99,** 181125 (2011).

31. Wirths, S. *et al.* Tensely strained GeSn alloys as optical gain media. *Appl. Phys. Lett.* **103,** 192110 (2013).

32. Wirths, S. *et al.* Band engineering and growth of tensile strained Ge/(Si)GeSn heterostructures for tunnel field effect transistors. *Appl. Phys. Lett.* **102,** 192103 (2013).

33. Gencarelli, F. *et al.* Crystalline Properties and Strain Relaxation Mechanism of CVD Grown GeSn. *ECS J. Solid State Sci. Technol.* **2,** P134–P137 (2013).

34. Gerthsen, D., Biegelsen, D., Ponce, F. A. & Tramontana, J. C. Misfit dislocations in GaAs heteroepitaxy on (001) Si. *J. Cryst. Growth* **106,** 157–165 (1990).

35. Sun, X., Liu, J., Kimerling, L. C. & Michel, J. Direct gap photoluminescence of n-type tensile-strained Ge-on-Si. *Appl. Phys. Lett.* **95,** 011911 (2009).

36. Ryu, M.-Y., Harris, T. R., Yeo, Y. K., Beeler, R. T. & Kouvetakis, J. Temperature-dependent photoluminescence of Ge/Si and $Ge_{1-y}Sn_y$/Si, indicating possible indirect-to-direct bandgap transition at lower Sn content. *Appl. Phys. Lett.* **102,** 171908 (2013).

37. Geiger, R. *et al.* Excess carrier lifetimes in Ge layers on Si. *Appl. Phys. Lett.* **104,** 062106 (2014).

38. Shaklee, K. L., Nahory, R. E. & Leheny, R. F. Optical gain in semiconductors. *J. Lumin.* **7,** 284–309 (1973).

Acknowledgements

The authors acknowledge the hospitality from the IR beamline of the SLS, where the photoluminescence experiments were performed. Part of this work has been funded by the Swiss National Science Foundation (SNF). This research received funding for CVD growth investigations from the European Community's Seventh Framework Programme under grant agreement No. 619509 (project E2SWITCH) and the BMBF project UltraLowPow (16ES0060K).

Author Contributions

J.M.H. fabricated the Ge/Si substrates. S.W. and D.B. planned the GeSn epitaxial growth experiments and S.W. and N.v.d.D. fabricated the GeSn/Ge/Si samples. M.L. and S.C. carried out the TEM measurements and analysis. S.W., D.B, G.M., N.v.d.D. and T.S. carried out crystal structure analysis including strain determination employing XRD and RBS. Z.I. performed the band structure simulations. S.W. and R.G. performed the optical measurements. R.G. and H.S. performed the JDOS modelling, gain analysis, and mode simulations. R.G. processed the GeSn cavities. S.M., J.F., D.B., H.S. and D.G. supervised the experiments and coordinated data interpretation. S.W., H.S., R.G. and D.B. wrote the paper. All authors discussed the results and commented on the manuscript.

Additional information

Supplementary information is available in the online version of the paper. Reprints and permissions information is available online at www.nature.com/reprints. Correspondence and requests for materials should be addressed to S.W. (s.wirths@fz-juelich.de) and D.B. (d.m.buca@fz-juelich.de)

Competing financial interests

The authors declare no competing financial interests.

Figure 1: **Crystal quality and dislocation analysis.** (a) Cross sectional transmission electron micrograph (TEM) of $Ge_{0.874}Sn_{0.126}$ (sample D). (b) Dislocation loops emitted below the $Ge_{0.874}Sn_{0.126}$/Ge interface penetrating only into the Ge buffer. (c) High resolution TEM of the interface used for Burgers vector calculations. Lomer dislocations with b = a/2[110] are identified.

Figure 2: **Temperature dependent photoluminescence measurements and modelling.** (a) Temperature-dependent PL spectra for samples A to D. (b) Integrated PL intensities normalized to the corresponding intensity at RT. The coloured curves show the result of a PL intensity simulation that includes the calculation of the joint density of states (JDOS) with the band offset ΔE between the minima of the $\Gamma-$ and the L-valley being the key fitting parameter. (c) ΔE as a function of the Sn concentration. The indirect-to-direct bandgap transition is found at approx. 9 % Sn for unstrained layers using 7.7 eV per unit of strain for the extrapolation.

Figure 3: **Optical gain determination via the variable stripe length method.** (a) Amplified spontaneous emission (ASE) spectra obtained from the 560 nm $Ge_{0.874}Sn_{0.126}$ layer (sample E) excited over lengths L between 50 and 400 µm at 595 kW/cm^2. The inset shows the calculated intensity of the fundamental TE mode (colour-coded) within a 5 µm wide, 900 nm steep waveguide structure revealing an overlap with the GeSn layer of 60 %. (b) The top part of the figure displays the decreasing full width at half maximum (FWHM) of the spectra presented in (a) with increasing stripe length L. Below, the ASE intensities for the peak energies (551 meV and 558 meV) are fit using $I_{ASE} = I_{O.} + \frac{I_{SP.}}{g}[\exp(g \cdot L) - 1]$ to determine the modal gain that is plotted in (c) as a function of the excitation. In red, the modal gain is

shown as obtained from the lasing threshold observed in homogeneously excited Fabry-Perot waveguide cavities with lengths of 250 µm, 500 µm and 1 mm.

Figure 4: **Optically pumped direct bandgap GeSn laser.** (a) Power-dependent PL spectra of a 5 µm wide and 1 mm long Fabry-Perot waveguide cavity fabricated from sample E (d_{GeSn} = 560 nm, 12.6 % Sn). The inset displays the temperature-dependent (20 K – 100 K) PL spectra at 1000 kW/cm^2 excitation density. (b) The integrated PL intensity as a function of optical excitation for waveguide lengths L_C = 250 µm, 500 µm and 1 mm. The inset shows the FWHM around the lasing threshold for the 1 mm long GeSn waveguide. (c) High resolution spectra of a 250 µm and a 500 µm long waveguide taken at 500 kW/cm^2. The mode spacing amounts to 0.50 meV and 0.27 meV which corresponds to a group refractive index of approximately 4.5 for the lasing mode. The pump laser homogeneously excites the waveguide cavity; the light emitted from one of the etched facets is analysed (inset).

Table I: **Layer properties, band structure parameters and effective masses.**

Sample	$a_{par.}$(Å) ± 0.01	$a_{perp.}$ (Å) ± 0.01	$x_{Sn,XRD}$ (%) ± 0.3	$x_{Sn,RBS}$ (%) ± 0.5	ε_{XRD} (%)	$\Delta E_{exp.}$ (meV)	$\Delta E_{calc.}$ (meV)
A	5.688	5.757	8.0	8.0	-0.70	-80	-50
B	5.712	5.765	9.6	10.3	-0.52	-10	-8
C	5.731	5.773	11.1	11.5	-0.41	-5	26
D	5.727	5.799	12.6	13.0	-0.71	25	28
E	5.735	5.776	12.6	13.0	-0.57	25	39

Here, $a_{par.}$ and a_{perp} are the in-plane and out-of-plane lattice constants, $\Delta E_{exp.}$ and $\Delta E_{calc.}$ are the band offsets between Γ and L valleys extracted from the JDOS model and calculated from the deformation potentials.

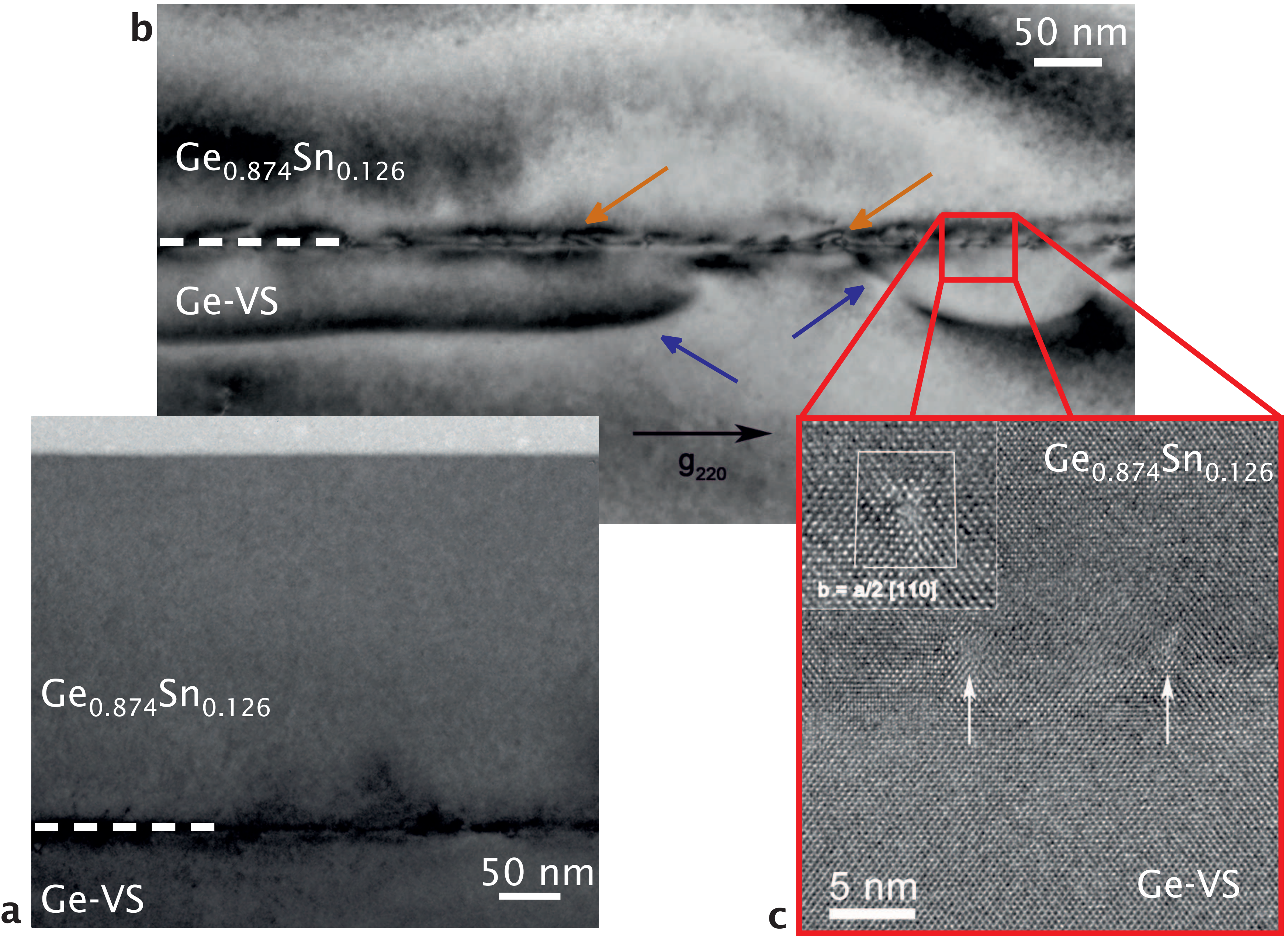

b
50 nm
$Ge_{0.874}Sn_{0.126}$
Ge-VS
g_{220}
a
$Ge_{0.874}Sn_{0.126}$
50 nm
Ge-VS
c
$Ge_{0.874}Sn_{0.126}$
b = a/2 [110]
5 nm
Ge-VS

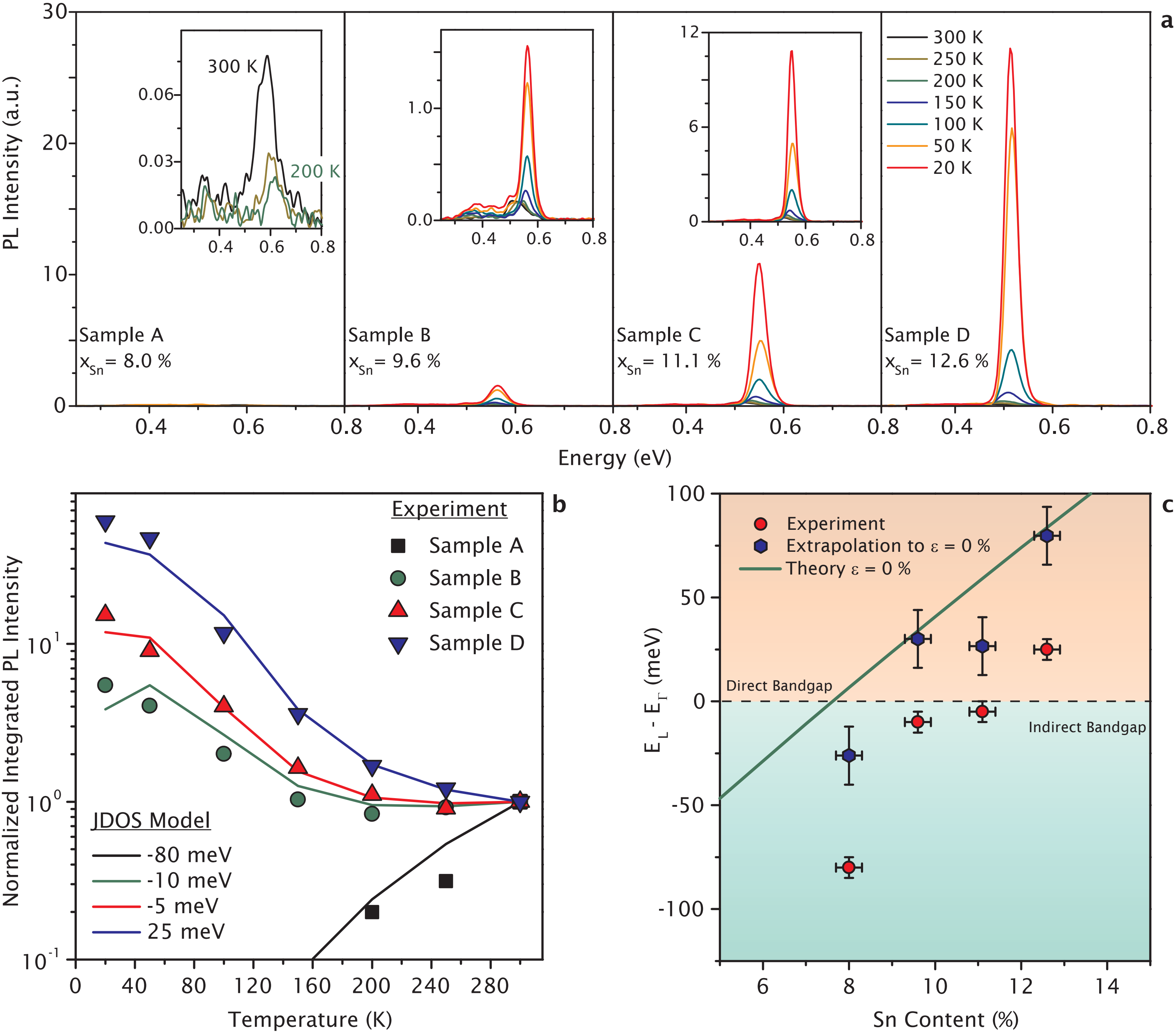

a
PL Intensity (a.u.)
Energy (eV)
300 K
200 K
Sample A
x_{Sn}= 8.0 %
Sample B
x_{Sn}= 9.6 %
Sample C
x_{Sn}= 11.1 %
Sample D
x_{Sn}= 12.6 %
300 K
250 K
200 K
150 K
100 K
50 K
20 K
b
Experiment
Sample A
Sample B
Sample C
Sample D
JDOS Model
-80 meV
-10 meV
-5 meV
25 meV
Normalized Integrated PL Intensity
Temperature (K)
c
Experiment
Extrapolation to ε = 0 %
Theory ε = 0 %
Direct Bandgap
Indirect Bandgap
$E_L - E_\Gamma$ (meV)
Sn Content (%)

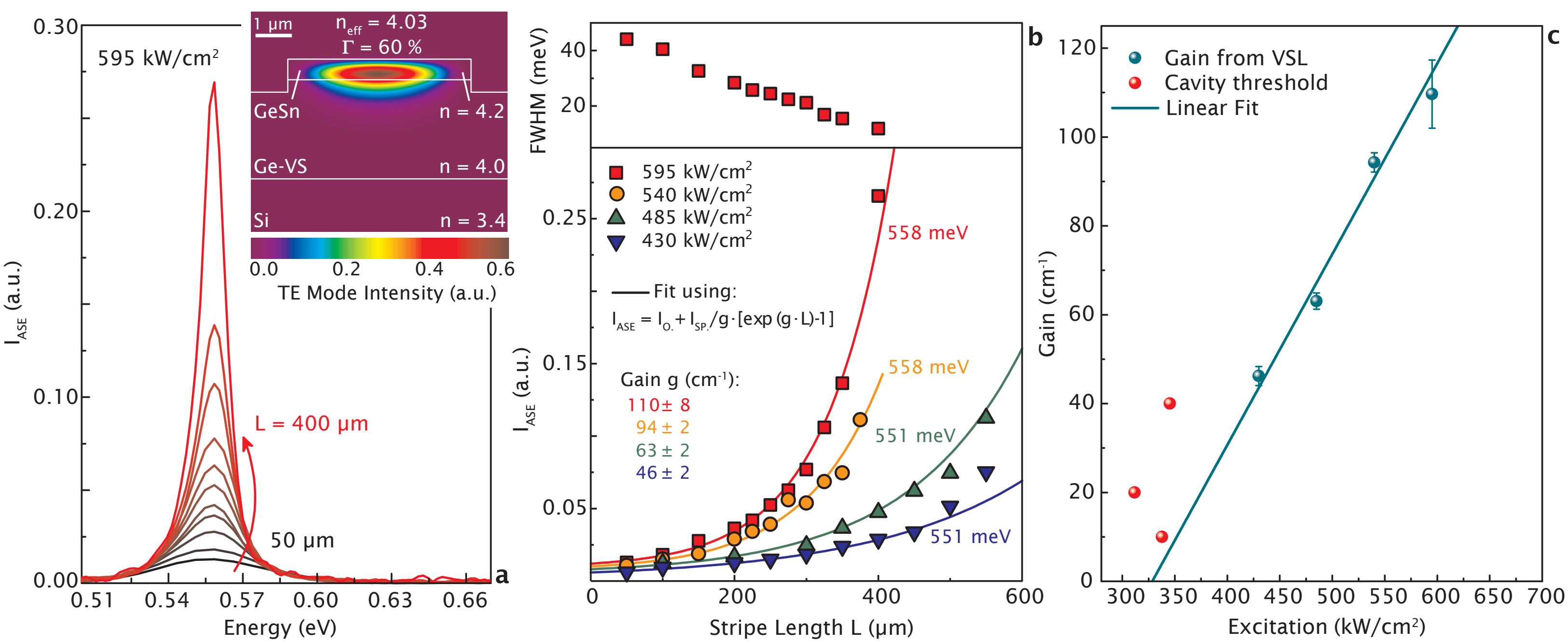

595 kW/cm²
1 µm
n_eff = 4.03
Γ = 60 %
GeSn
n = 4.2
Ge-VS
n = 4.0
Si
n = 3.4
0.0
0.2
0.4
0.6
TE Mode Intensity (a.u.)
L = 400 µm
50 µm
I_ASE (a.u.)
Energy (eV)
a
FWHM (meV)
b
595 kW/cm²
540 kW/cm²
485 kW/cm²
430 kW/cm²
Fit using:
I_ASE = I_O + I_SP/g·[exp(g·L)-1]
Gain g (cm⁻¹):
110± 8
94 ± 2
63 ± 2
46 ± 2
558 meV
558 meV
551 meV
551 meV
Stripe Length L (µm)
c
Gain from VSL
Cavity threshold
Linear Fit
Gain (cm⁻¹)
Excitation (kW/cm²)

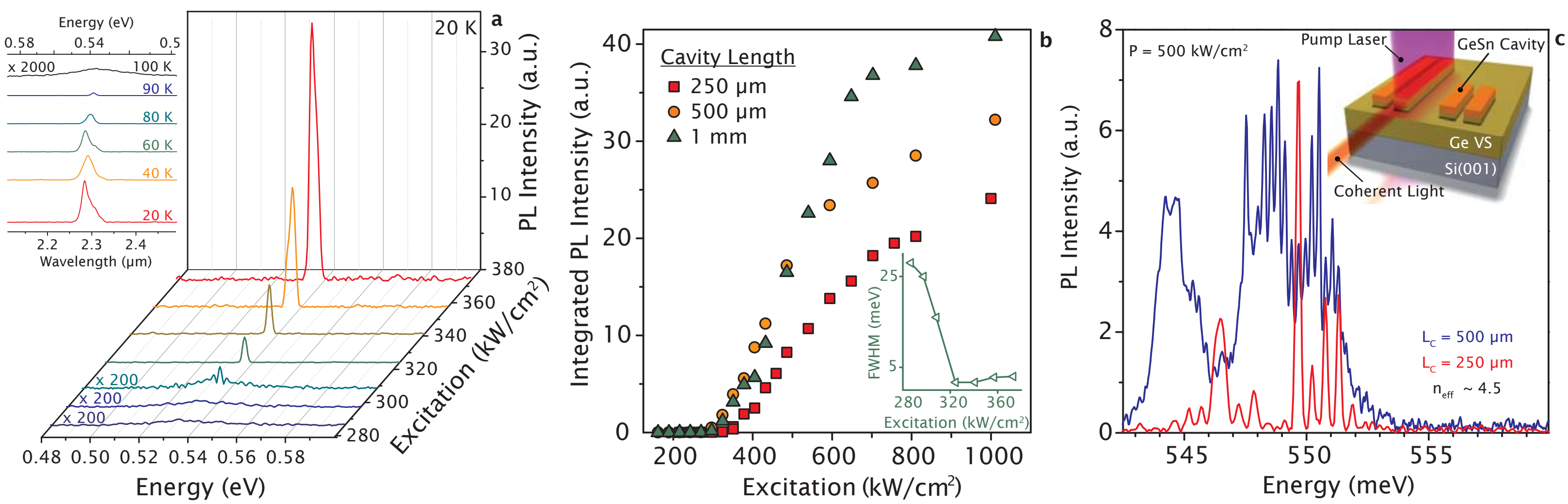

a
20 K
PL Intensity (a.u.)
Excitation (kW/cm²)
Energy (eV)
Energy (eV)
Wavelength (µm)
x 2000
100 K
90 K
80 K
60 K
40 K
20 K
x 200
x 200
x 200
b
Integrated PL Intensity (a.u.)
Cavity Length
250 µm
500 µm
1 mm
FWHM (meV)
Excitation (kW/cm²)
Excitation (kW/cm²)
c
P = 500 kW/cm²
Pump Laser
GeSn Cavity
Ge VS
Si(001)
Coherent Light
PL Intensity (a.u.)
L_C = 500 µm
L_C = 250 µm
n_eff ~ 4.5
Energy (meV)